CHEMISTRY
A EUROPEAN JOURNAL

DOI: 10.1002/chem.200903023

Structural Characterisation of the Li Argyrodites Li_7PS_6 and Li_7PSe_6 and their Solid Solutions: Quantification of Site Preferences by MAS-NMR Spectroscopy

Shiao Tong Kong,[a] Özgül Gün,[a] Barbara Koch,[b] Hans Jörg Deiseroth,*[a] Hellmut Eckert,*[b] and Christof Reiner[a]

Dedicated to Professor Dr. Gerd Becker on the occasion of his 70th birthday

Abstract: Li_7PS_6 and Li_7PSe_6 belong to a class of new solids that exhibit high Li^+ mobility. A series of quaternary solid solutions $Li_7PS_{6-x}Se_x$ $(0 \le x \le 6)$ were characterised by X-ray crystallography and magic-angle spinning nuclear magnetic resonance (MAS-NMR) spectroscopy. The high-temperature (HT) modifications were studied by single-crystal investigations (both $F\bar{4}3m$, $Z=4$, Li_7PS_6: $a=9.993(1)$ Å, Li_7PSe_6: $a=10.475(1)$ Å) and show the typical argyrodite structures with strongly disordered Li atoms. HT-Li_7PS_6 and HT-Li_7PSe_6 transform reversibly into low-temperature (LT) modifications with ordered Li atoms. X-ray powder diagrams show the structures of LT-Li_7PS_6 and LT-Li_7PSe_6 to be closely related to orthorhombic LT-α-Cu_7PSe_6. Single crystals of the LT modifications are not available due to multiple twinning and formation of antiphase domains. The gradual substitution of S by Se shows characteristic site preferences closely connected to the functionalities of the different types of chalcogen atoms (S, Se). High-resolution solid-state ^{31}P NMR is a powerful method to differentiate quantitatively between the distinct $(PS_{4-n}Se_n)^{3-}$ local environments. Their population distribution differs significantly from a statistical scenario, revealing a pronounced preference for P–S over P–Se bonding. This preference, shown for the series of LT samples, can be quantified in terms of an equilibrium constant specifying the melt reaction $Se_P + S^{2-} \rightleftharpoons S_P + Se^{2-}$, prior to crystallisation. The ^{77}Se MAS-NMR spectra reveal that the chalcogen distributions in the second and third coordination sphere of the P atoms are essentially statistical. The number of crystallographically independent Li atoms in both LT modifications was analysed by means of $^6Li\{^7Li\}$ cross polarisation magic angle spinning (CPMAS).

Keywords: argyrodites · chalcogens · lithium · NMR spectroscopy · phase transitions · phosphorus · structure elucidation

Introduction

The search for high-performance solid electrolytes suitable for lithium ion batteries has prompted considerable research activity in the area of fast lithium ion conductors. Based on earlier reports about high Ag and Cu ionic conductivities in solids of the Ag and Cu argyrodite families,[1,2] we recently discovered a promising new class of Li-rich materials ("Li argyrodites") with high Li ionic mobility. Although synthetic efforts to replace Ag in the mineral "argyrodite" Ag_8GeS_6 by Li were not successful, a series of closely related Li argyrodites with the composition Li_6PS_5X (X = Cl, Br, I) could be obtained by solid-state syntheses[3,4] and were characterised by single-crystal X-ray diffraction, magic-angle spinning nuclear magnetic resonance (MAS-NMR) and frequency dependent conductivity measurements. These investigations have revealed a wide spectrum of possibilities for available compounds. Among those are halide-free ternary solids of the type Li_7PCh_6 (Ch = S, Se) and the corresponding solid solutions. Moreover, it became clear that, in addition to the chemical composition, the microstructure of the respective

[a] S. T. Kong, Ö. Gün, Prof. Dr. H. J. Deiseroth, Dr. C. Reiner
University of Siegen, Inorganic Chemistry I
Adolf Reichwein Strasse 2, 57068 Siegen (Germany)
Fax: (+49) 271-740-2555
E-mail: deiseroth@chemie.uni-siegen.de

[b] B. Koch, Prof. Dr. H. Eckert
Institut für Physikalische Chemie
Westfälische Wilhelms-Universität Münster
Corrensstrasse 30, 48149 Münster (Gemany)
Fax: (+49) 251-83-29159
E-mail: eckerth@uni-muenster.de

materials with respect to grain size, packing density, structural defects and so forth is crucial for their properties regarding potential practical applications as Li electrolytes in solid-state devices. This is, in particular, relevant with respect to earlier reports about high Li conductivities ($\sigma \approx 10^{-3}\,S\,cm^{-1}$) in glassy Li_2S–P_2S_5 systems with compositions of $\approx 0.8\,Li_2S/0.2\,P_2S_5$ obtained by high-energy ball milling.[5] Although the microstructure of such systems on a nm scale is not fully clear, the partial formation of ordered domains ($< 10\,\mu m$) with structural properties similar to crystalline argyrodites is likely.

With increasing knowledge about Li argyrodites, it became more and more clear that the crystalline Li argyrodites undergo temperature driven order–disorder (o–d) transitions, an experimental observation that has not yet been reported for the just mentioned glassy systems. In the case of the known crystalline Ag and Cu argyrodites, the corresponding phase transitions were sometimes overlooked or not referenced. Moreover, it turned out that the o–d transitions are considerably shifted to lower temperatures or even completely suppressed in suitable solid solutions of different types.

In this paper, we present comprehensive X-ray diffraction and solid-state NMR studies of the structural and phase transition properties of the two ternary argyrodites Li_7PCh_6 (Ch = S, Se) and their solid solutions $Li_7PS_{6-x}Se_x$ ($0 < x < 6$). For the cubic, high-temperature (HT) phases, HT-Li_7PCh_6, of the two ternary compounds, the results of X-ray single-crystal investigations are presented. The structural characterisations of the low-temperature (LT) modifications are restricted to less significant X-ray powder data due to pronounced multiple twinning upon the phase transformation. The MAS-NMR experiments are based on the LT modifications at ambient temperatures, in which special emphasis is put on the positional mixing between S and Se atoms in the solid solutions $Li_7PS_{6-x}Se_x$ and the number of crystallographically independent Li atoms in the LT structures. In the interpretation of the MAS-NMR results, one has to consider that the orthorhombic LT structure is most likely very similar but not completely identical to the cubic HT structures. In particular the spatial distribution and individual coordination of the Li atoms differs between HT and LT, whereas the P/Ch distributions, on which the MAS-NMR experiments are focussed, are very similar.

Results and Discussion

General properties of the argyrodite structure type: The interpretation of the MAS-NMR and X-ray results of this paper does not require an understanding of detailed structural properties that favour the high mobility of M^+ (M = Li, Cu, Ag) in argyrodites and make this class of materials so attractive. Some essentials, however, referring to a "reference argyrodite" of the general composition Li_7PCh_6 (Ch = S, Se) as an example are given below in order to simplify an understanding of the most important structural aspects.

The great majority of argyrodites crystallise in high-temperature modifications ($F\bar{4}3m$, $Z = 4$) and at least one low-temperature modification. In both modifications, the arrangement of the chalcogen atoms is important in order to rationalise essential structural and physical properties. The partial structure of the chalcogen atoms corresponds to a tetrahedral close packing similar to the arrangement of Mg and Cu atoms in the cubic Laves phase $MgCu_2$ ($Fd\bar{3}m$).[6,7] The resulting three-dimensional structure offers a dense system of 136 distorted tetrahedra per cubic unit cell with corner, edge and face sharing. Four tetrahedra per unit cell, which are not interconnected directly, are occupied by P atoms forming tetrahedral $(PCh_4)^{3-}$ groups. A pronounced static–dynamic disorder over the remaining tetrahedral holes is observed for the Li atoms. Upon cooling, a disorder–order transition driven by a freezing out of the disordered Li atoms occurs, which is accompanied by pronounced multiple twinning and formation of antiphase domains. Hence, the freezing out of the Li atoms in the LT phase and the associated relaxation of the tetrahedral framework of chalcogen atoms has to be studied by powder rather than by single-crystal investigations. According to the present knowledge, the relaxation of the P–Ch partial structure is small in spite of a significant symmetry lowering upon formation of the LT phase. Although, in the HT modification, the resulting 132 empty tetrahedra are basically accessible for the 28 disordered Li atoms, they are ordered in the LT modifications.

For discussions of the MAS-NMR results obtained for HT-Li_7PCh_6 (Ch = S, Se) and discussed in this paper, it is primarily important to visualise the argyrodite structure in a way that illustrates the spatial distribution of the chalcogen atoms with respect to one of the four PCh_4 tetrahedra per unit cell. Figure 1 shows that Ch1 (Wyckoff position 16*e*) forms the Ch atoms of the four PCh_4 groups. The Ch2 (4*c*) atom constitutes the second and Ch3 (4*a*) the third coordination sphere. This crystal chemical picture also holds for all LT modifications of argyrodites described so far, although a small but significant symmetry reduction is observed, pri-

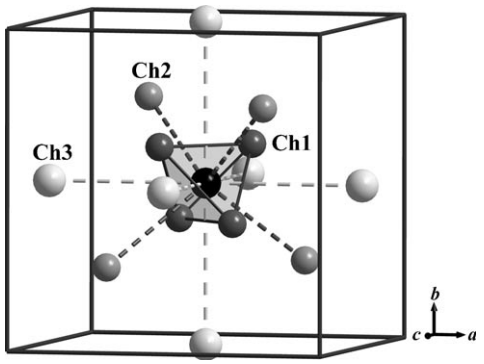

Figure 1. Unit cell of HT-Li_7PCh_6 argyrodites (Li positions are omitted) emphasising one of the four PCh_4 groups per unit cell with Ch atoms of the second and third coordination spheres. In the LT modification the P/Ch partial structure (but *not* the Li partial structure) is most likely very similar.

marily caused by ordering of the Li/Cu atoms (e.g., Ch1 splits into four independent Wyckoff positions in the LT phase of LT-α-Cu_7PSe_6).[8,9]

X-ray and thermal investigations of the solid solutions $Li_7PS_{6-x}Se_x$: Li_7PS_6 and Li_7PSe_6 were described in two earlier publications based on powder X-ray, differential scanning calorimetry (DSC) and NMR spectroscopy.[10,11] Moreover, Li_7PS_6 was mentioned in a systematic X-ray study of ternary Li/P/S compounds, but without mentioning the existence of HT and LT forms.[12] Due to the low scattering power of Li, Rietveld refinements of the crystal data of the LT modifications (powder data only) were not successful up to now. Instead, we are restricted to comparisons with published crystal structures of structurally related LT modifications of Cu and Ag argyrodites[9,13] (e.g., LT-α-Cu_7PSe_6).

HT-Li_7PS_6 and HT-Li_7PSe_6 ($F\bar{4}3m$, $Z=4$): The structural data obtained from the two high-temperature measurements (Tables 1–3) clearly confirmed space group $F\bar{4}3m$, which is typical for HT argyrodites in general. Weak but significant residual electron density obtained by difference density calculations based on the Fourier coefficients defined by the P and Ch contributions can be assigned to Li atoms in the Wyckoff position 48*h* (reduced occupancy, Table 2) in both cases. This crystallographic split position is also characteristic in, for example, disordered Cu^+ in HT-γ-Cu_7PSe_6[8] and comparable argyrodites with other chemical compositions. It is representative for the two end points of an ellipsoidal electron density distribution that extends between the centres of two face-sharing tetrahedra. A simultaneous occupation of both positions in the real structure is impossible due to an unreasonable short Li–Li distance of about 100 pm. The P–S and P–Se distances of ≈204 and ≈220 pm for HT-Li_7PS_6 and HT-Li_7PSe_6, respectively, agree perfectly with the average values observed in the compounds Li_3PS_4 (P–S = 205 pm[14]) and K_3PSe_4[15] (P–Se = 220 pm), respectively. The average distances Li–S (252 pm) and Li–Se (264 pm) based on the split position 48*h* for Li seem to be slightly increased in comparison to values found for Li_3PS_4 (Li–S = 244–251 pm) and Li_2Se[16] (Li–Se = 260 pm), respectively, with ordered Li atoms.

Table 1. Summary of data collection and refinement details for HT-Li_7PS_6 and HT-Li_7PSe_6.

	Li_7PS_6	Li_7PSe_6
M_r [g mol^{-1}]	271.91	553.3
crystal system	cubic	Cubic
space group	$F\bar{4}3m$	$F\bar{4}3m$
Z	4	4
colour	colourless	Orange
crystal dimension [mm^3]	0.10×0.07×0.045	0.22×0.08×0.03
a [Å]	9.993(1)	10.475(1)
V [Å^3]	997.8(2)	1149.4(2)
ρ_{calcd} [g cm^{-3}]	1.81	3.2
μ [mm^{-1}]	1.45	19.17
F (000)	528	960
T [K]	503	453
θ range [°]	3.53–30.44	3.37–30.13
index ranges	$-14 \le h \le 14$	$-14 \le h \le 14$
	$-14 \le k \le 14$	$-14 \le k \le 14$
	$-14 \le l \le 14$	$-14 \le l \le 14$
measured reflections	3757	3484
independent reflections	188	214
completeness to θ (%)	100	100
$R_{int.}$	0.0308	0.0532
data/restraints/parameter	188/0/12	214/0/12
R values [$I \ge 2\sigma(I)$]	$R_1 = 0.0278$	$R_1 = 0.0268$
	$wR_2 = 0.069$	$wR_2 = 0.0429$
R values (all data)	$R_1 = 0.0319$	$R_1 = 0.0378$
	$wR_2 = 0.0706$	$wR_2 = 0.0445$
A[a]	0.0479	0.0215
GooF	1.183	1.141
ρ_{max} [eÅ^{-3}]	0.211	0.483
ρ_{min} [eÅ^{-3}]	−0.221	−0.290

[a] Weighting scheme: $w = 1/[\sigma^2(F_o^2) + (AP)^2 + BP]$, $P = (F_o^2) + 2F_c^2)/3$; $B = 0$ for both samples.

Table 2. Wyckoff positions, coordinates, equivalent displacement parameters U_{eq} [Å^2] and occupancies for HT-Li_7PS_6 and HT-Li_7PSe_6 (bold).

Atom	Site	X	y	z	U_{eq}	Occupancy
P	4*b*	0.5	*x*	*x*	0.0301(5)	1
		0.5	***x***	***x***	**0.031(1)**	**1**
S1	16*e*	0.61808(7)	*x*	*x*	0.0425(4)	1
Se1		**0.62150(9)**	***x***	***x***	**0.0464(3)**	**1**
S2	4*c*	0.25	*x*	*x*	0.0358(5)	1
Se2		**0.25**	***x***	***x***	**0.0392(6)**	**1**
S3	4*a*	0	*x*	*x*	0.0470(6)	1
Se3		**0**	***x***	***x***	**0.0473(7)**	**1**
Li	48*h*	0.817(2)	0.476(3)	0.683(1)	0.12(1)	0.53(5)
		0.823(2)	**0.479(3)**	**0.677(2)**	**0.10(1)**	**0.66(5)**

Table 3. Selected interatomic distances for HT-Li_7PS_6 and HT-Li_7PSe_6.

	Li_7PS_6	Li_7PSe_6
Li–Ch1 (2×)	2.53(2)	2.65(2)
Li–Ch2	2.45(3)	2.63(3)
Li–Ch3	2.60(2)	2.63(2)
average	2.53(2)	2.64(2)
P–Ch (4×)	2.044(1)	2.204(2)

LT-Li_7PS_6 and LT-Li_7PSe_6: There is significant evidence from the X-ray powder diagrams that the crystal structures of LT-Li_7PS_6 and LT-Li_7PSe_6 are very similar if not isotypic to the structure of orthorhombic LT-α-Cu_7PSe_6. This can be seen in Figure 2, in which experimental powder diagrams of LT-Li_7PS_6 and LT-Li_7PSe_6 are compared with calculated ones based on the atomic positions of LT-α-Cu_7PSe_6[9] and adjusted lattice constants. In contrast to this structure model, which implies only one crystallographically independent P position, the subsequently presented NMR experiments on these compounds give evidence for the presence of two slightly different P positions for LT-Li_7PS_6 and LT-Li_7PSe_6 (see below). It was not possible to resolve this discrepancy up to now. Cyclic heating and cooling experiments on powder samples monitored by X-ray diffraction, clearly demonstrate reversible phase transitions with transition temperatures of 483 K (Li_7PS_6, Figure 3) and 437 K (Li_7PSe_6).

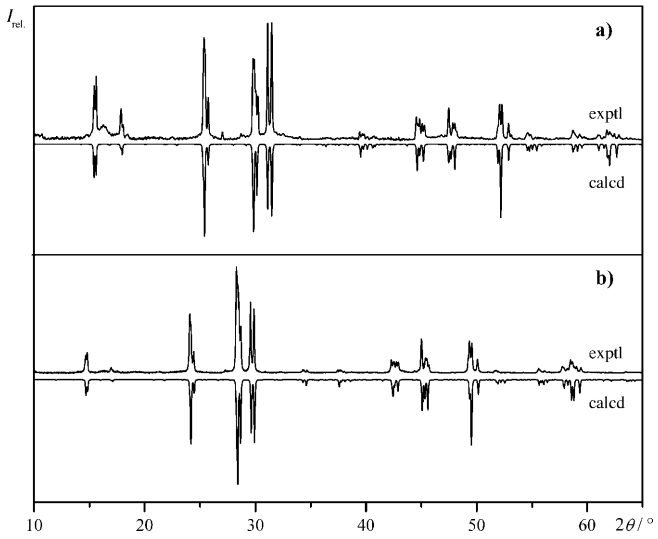

Figure 2. Experimental powder patterns of LT-Li_7PS_6 (a) and LT-Li_7PSe_6 (b) in comparison to calculated diagrams based on the structure parameters of LT-α-Cu_7PSe_6[9] (space group $Pna2_1$, no. 33) with adjusted lattice constants (LT-Li_7PS_6: $a=14{,}076(6)$ Å, $b=6.917(2)$ Å, $c=9{,}955(4)$ Å; LT-Li_7PSe_6: $a=14.760(2)$ Å, $b=7.270(8)$ Å, $c=10.448(2)$ Å, $T=298$ K,). Positional parameters[9] (all in Wyckoff position 4*a*): P: 0.124, 0.753, 0.25; Ch1: 0.002, 0.757, 0.118; Ch2: 0.251, 0.251, 0.624; Ch3: 0.379, 0.504, 0.876; Ch4: 0.881, 0.505, 0.873; Ch5: 0.125, 0.718, 0.735; Ch6: 0.385, 0.740, 0.506; Li1: 0.238, 0.464, 0.998; Li2: 0.771, 0.416, 0.047; Li3: 0.294, 0.768, 0.745; Li4: 0.967, 0.092, 0.088; Li5: 0.551, 0.936, 0.928; Li6: 0.857, 0.021, 0.365; Li7: 0.377, 0.830, 0.270, (Ch = S, Se).

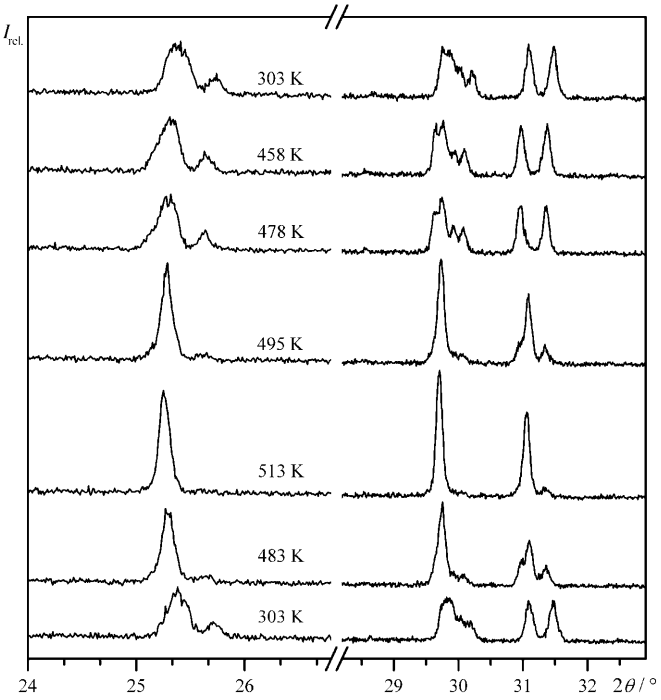

Figure 3. Sections of X-ray powder diagrams (Cu-$K_{\alpha 1}$) of Li_7PS_6 (heating–cooling cycle starting at 303 K) showing the reversible phase transition between the assumed orthorhombic LT and cubic HT modification ($T_t=$ 483 K from DSC measurement).

Solutions $Li_7PS_{6-x}Se_x$, X-ray and thermal analysis investigations: The series of powder X-ray diagrams of selected samples of $Li_7PS_{6-x}Se_x$ at ambient temperatures (Figure 4) clearly demonstrates that all of the structures can be assigned to the LT modification. The lattice parameters (Figure 5) of the solid-solution samples only show a small deviation from linearity. In DSC measurements of a solid-solution series of $Li_7PS_{6-x}Se_x$ up to 873 K, only one reversible thermal effect (HT↔LT, $387\text{ K} < T_t < 483$ K, Figure 6) with a significant hysteresis is visible. Additional thermal effects were not observed between the phase transition (T_t) and the melting point (>973 K). It is remarkable that T_t undergoes a minimum in the solid-solution sample $Li_7PS_2Se_4$ and is, in all cases, lower than for the ternary components Li_7PS_6 and Li_7PSe_6.

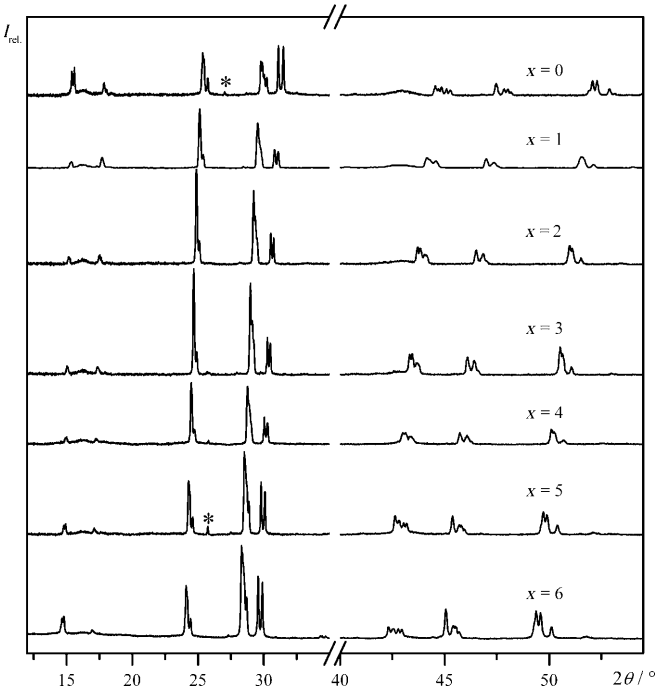

Figure 4. X-ray powder diagrams for $Li_7PS_{6-x}Se_x$ ($0 \le x \le 6$) samples show the continuous shift to smaller diffraction angles with increasing Se content and the typical pattern for the assumed orthorhombic LT modification. Minor impurities of Li_2(S/Se) are indicated with *.

^{31}P solid-state NMR spectroscopy: Figure 7 summarises the ^{31}P solid-state NMR results obtained on the whole set of $Li_7PS_{6-x}Se_x$ samples. The spectra obtained on the end members $x=0$ (LT and metastable HT forms at room temperature) and $x=6$ (LT) are in good agreement with earlier investigations.[10,11] In the present study, LT-Li_7PS_6 could be characterised for the first time. Surprisingly, the NMR spectra measured both on LT-Li_7PS_6 and LT-Li_7PSe_6 give clear evidence for the presence of two crystallographically different PCh_4 groups. This observation suggests that the space group assigned for the powder diffraction data on basis of LT-α-Cu_7PSe_6 cannot be completely correct, and that the

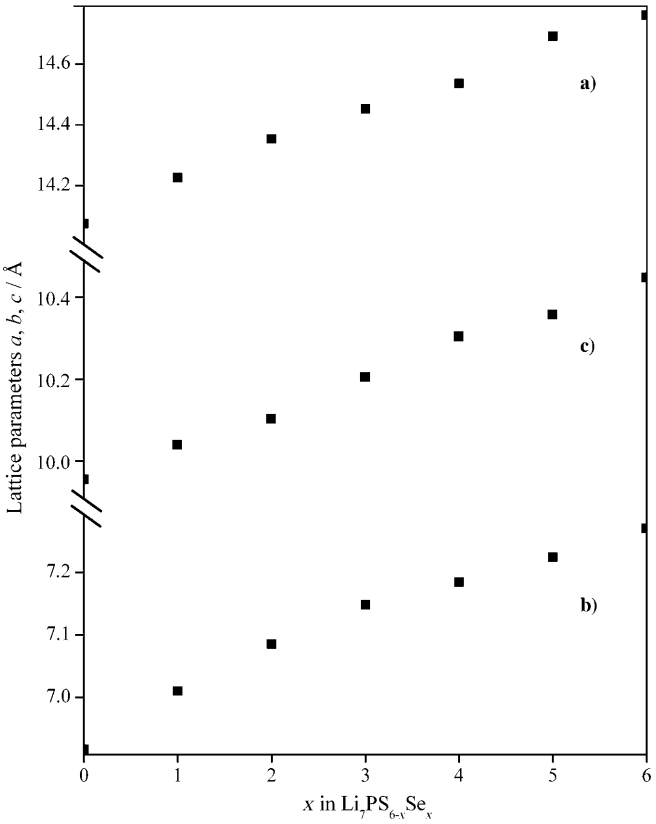

Figure 5. Graphical representation of the lattice constants of the solid solution series $Li_7PS_{6-x}Se_x$ ($0 \le x \le 6$).

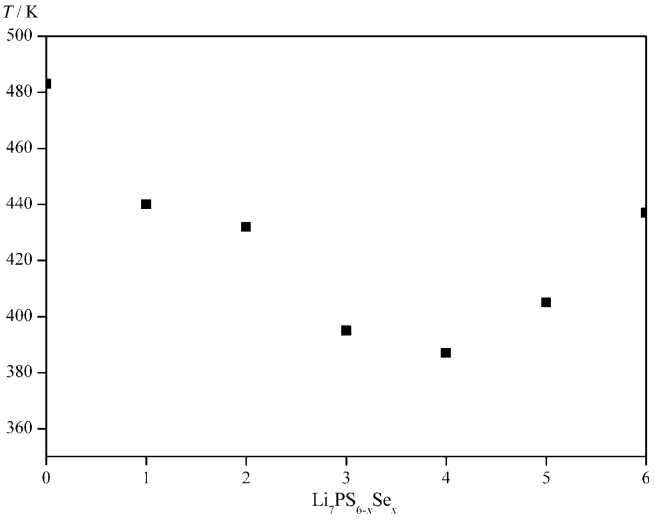

Figure 6. Change of the LT↔HT transition temperature for the solid-solution series $Li_7PS_{6-x}Se_x$ ($0 \le x \le 6$) from DSC experiments.

structures of the Li compounds must have lower symmetry. The small chemical shift differences (2.1 ppm for the sulfide, 3.1 ppm for the selenide) between the two resonances, however, indicate that the sites are chemically and crystallographically very similar. Further clarification of this apparent discrepancy requires detailed single-crystal structural

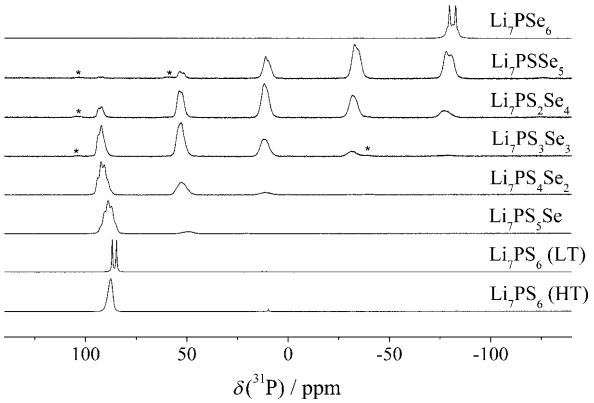

Figure 7. ^{31}P MAS-NMR spectra of $Li_7PS_{6-x}Se_x$ ($0 \le x \le 6$) solid solutions. Spinning sidebands are marked by asterisks. HT-Li_7PS_6 was obtained as a metastable phase at room temperature.

analysis data. For the selenide, the two principal resonances are flanked by minor signals attributable to indirect dipolar interactions of the phosphorus nuclei with directly bonded ^{77}Se neighbours. From a spectral simulation, we determined the isotropic scalar coupling constant $^1J(^{31}P,^{77}Se)$ to be 450 ± 10 Hz.

The spectra of the mixed $Li_7PS_{6-x}Se_x$ samples show characteristic five-peak patterns reflecting the presence of the five possible distinct $PS_{4-n}Se_n$ environments. Owing to the relatively broad line widths, hyperfine structures due to ^{31}P–^{77}Se indirect spin–spin coupling are not observable in this case. Closer inspection of these spectra reveals that each peak representing a particular $(PS_{4-n}Se_n)^{3-}$ environment seems to be comprised of multiple resonances. With the exception of the case of the $(PS_4)^{3-}$ units, in which this fine structure is clearly visible, the resolution is not sufficient to attempt more detailed line-shape analyses. For this reason, Table 4 summarises the observed average isotropic chemical shifts measured for each peak cluster. Regarding the resonance frequencies of the individual $PS_{4-n}Se_n$ environments, it is interesting to note that the ^{31}P chemical shift shows an approximately linear dependence on n, a situation rarely encountered in substitutional series of this kind. Table 4 also summarises the intensity distributions measured for each peak cluster in the five mixed compounds studied and compares these experimental data with the fractional peak areas expected from a scenario assuming statistical mixing of sulfur and selenium atoms over the three distinct chalcogen sites in the argyrodite lattice. For the latter scenario, the statistical probability $P(n,y)$ of a phosphorus atom being part of the first coordination sphere of phosphorus, that is, to be bonded to n Se atoms and $4-n$ S atoms ($0 \le n \le 4$) is given by Equation (1), in which y ($0 \le y \le 1$) represents the fractional contribution of Se to the total chalcogen inventory. Clearly, Table 4 and Figure 8 reveal that the chalcogen distribution in the first coordination sphere of phosphorus is not statistical; bonding to sulfur is strongly preferred over bonding to selenium. We can quantify this preference on the basis of an equilibrium constant postulated for a hy-

Table 4. ^{31}P chemical shifts of the individual $(PS_{4-n}Se_n)^{3-}$ resonances in $Li_7PS_{6-x}Se_x$ solid solutions. The experimental fractional areas (exptl) are compared to those expected from a statistical distribution (calcd).

		PS_4	PS_3Se	PS_2Se_2	$PSSe_3$	PSe_4
Li_7PSe_6	δ [ppm]					−79.6;−82.7
	% exptl	–	–	–	–	100
	% calcd					100
Li_7PSSe_5	δ [ppm]	93	53	10	−34	−79
	% exptl	0.6	6.3	20.8	38.1	34.2
	% calcd	0.1	1.5	11.6	38.6	48.2
$Li_7PS_2Se_4$	δ [ppm]	93	53	11	-33	−77
	% exptl	8.3	23.9	31.8	25.6	10.3
	% calcd	1.2	9.9	29.6	39.5	19.8
$Li_7PS_3Se_3$	δ [ppm]	92	53	12	−32	−78
	% exptl	29.3	36.9	22.8	9.2	1.8
	% calcd	6.3	25.0	37.5	25.0	6.3
$Li_7PS_4Se_2$	δ [ppm]	92[a]	52	11	–	–
	% exptl	63.1	29.5	7.4	–	–
	% calcd	19.8	39.5	29.6	9.9	1.2
Li_7PS_5Se	δ [ppm]	89[b]	49	–	–	–
	% exptl	92.2	7.8	–	–	–
	% calcd	48.2	38.6	11.6	1.5	0.1
LT-Li_7PS_6	δ [ppm]	86.9;84.7				
	% exptl	100	–	–	–	–
	% calcd	100				
HT-Li_7PS_6[c]	δ [ppm]	87.8				
	% exptl	100	–	–	–	–
	% calcd	100				

[a] Five components at 94.0, 92.4, 90.8, 88.9, and 87.2 ppm. [b] Five components at 92.7, 90.8, 88.9, 87.0, and 85.1 ppm. [c] Obtained metastable at room temperature.

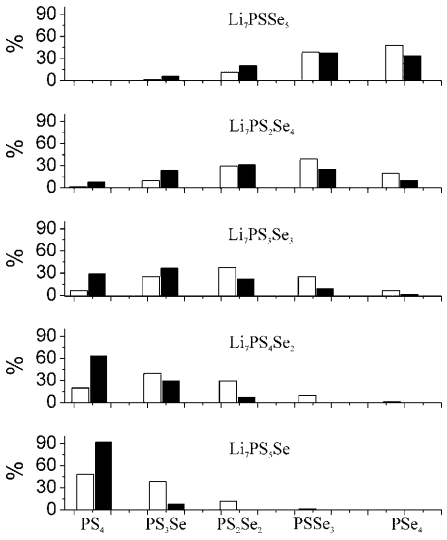

Figure 8. Intensity distribution $P(n,y)$ of the individual $(PS_{4-n}Se_n)^{3-}$ resonances. Black bars: experimental values determined by peak integration; white bars: values predicted from a statistical distribution scenario.

pothetical reaction [Eq. (2)], in which S_P and Se_P represent the P-bonded sulfur and selenium atoms, respectively, which are in equilibrium with the free sulfide and selenide ions in the melts from which these solid solutions crystallise. Based on the NMR data we can calculate the equilibrium constant for this reaction by using Equation (3). The mole fractions $[Se_P]$ and $[S_P]$ follow from the experimental distributions $P(n,y)$ according to Equations (4) and (5). Conversely, the mole fractions $[Se^{2-}]$ and $[S^{2-}]$ of the free chalcogenide ions follow from Equations (6) and (7). Table 5 summarises the

Table 5. Equilibrium constants K calculated from the experimental $P(n,y)$ values for $Li_7PS_{6-x}Se_x$ solid solutions.

Li_7PSSe_5	$Li_7PS_2Se_4$	$Li_7PS_3Se_3$	$Li_7PS_4Se_2$	Li_7PS_5Se
–	31	28	30	43

K values thus calculated. Consistent results were obtained for four of the five argyrodite solid solutions, quantitatively characterising the bonding preference of phosphorus with sulfur over selenium.

$$P(n,y) = 4!/(n!(4-n)!)y^n(1-y)^{4-n} \quad (1)$$

$$Se_P + S^{2-} \rightleftharpoons S_P + Se^{2-} \quad (2)$$

$$K = \{[S_P][Se^{2-}]\}/\{[Se_P][S^{2-}]\} \quad (3)$$

$$[Se_P] = \{4 \times P(4,y) + 3 \times P(3,y) + 2 \times P(2,y) + 1 \times P(1,y)\} \quad (4)$$

$$[S_P] = \{4 \times P(0,y) + 3 \times P(1,y) + 2 \times P(2,y) + 1 \times P(3,y)\} \quad (5)$$

$$[Se^{2-}] = \{6y-[Se_P]\} \quad (6)$$

$$[S^{2-}] = \{6(1-y)-[S_P]\} \quad (7)$$

Finally, the perceptible fine structure, which is particularly pronounced for the $(PS_4)^{3-}$ environments, has not yet been explained. We attribute it to the distribution of the chalcogenide ions in the second coordination sphere of the phosphorus atoms. Figures 9 and 10 show a representative peak deconvolution into the five possible environments. These results can again be compared with a random distribution scenario calculated using Equation (1). In this case, the relevant value of y follows from the concentrations $[Se^{2-}]$ and $[S^{2-}]$ [from Eq. (6) and (7)] that are available for occupying the second coordination sphere of phosphorus. Figure 9 suggests that the chalcogen occupancy of this site with sulfur or selenium is quite close to random in Li_7PS_5Se, whereas in $Li_7PS_4Se_2$ there seems to be some deviation from randomness (Figure 10).

^{77}Se solid-state NMR spectroscopy: Previous ^{77}Se NMR studies of the argyrodite Ag_7PSe_6[17] were able to clearly differentiate the three crystallographically distinct selenium environments. Although the P-bonded selenium atoms are characterised by wide spinning sideband patterns signifying a strongly anisotropic chemical shift tensor, the resonances attributed to selenium atoms in the 4*a* and 4*c* positions reveal essentially isotropic shielding. Similar results were obtained on the mixed chalcogenides of the present study;

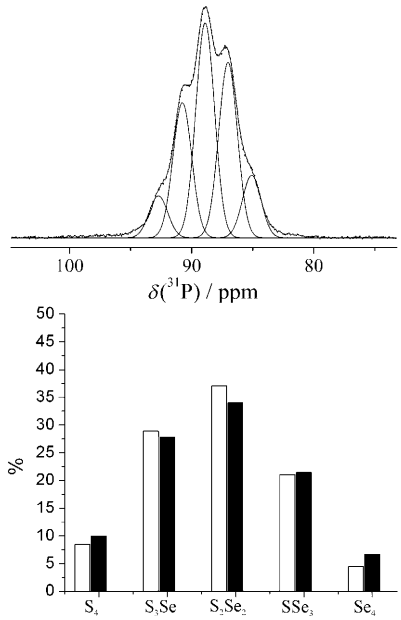

Figure 9. Peak deconvolutions of the $(PS_4)^{3-}$ resonance in Li_7PS_5Se. Solid bars show the experimental intensity distributions for the chalcogen configuration in the 4*c* position (second coordination sphere of phosphorus); open bars show the expected intensity distribution based on a statistical scenario.

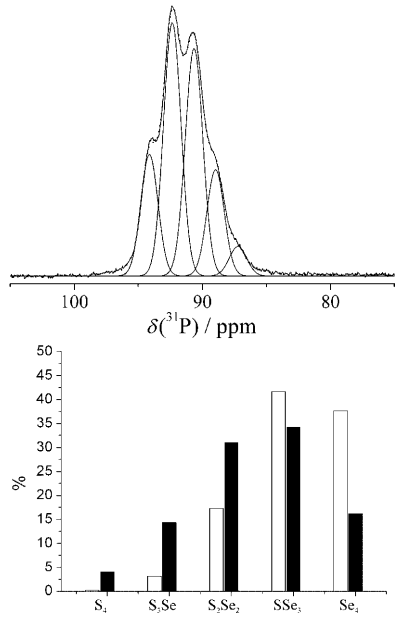

Figure 10. Peak deconvolution of the $(PS_4)^{3-}$ resonance in $Li_7PS_4Se_2$. Solid bars show the experimental intensity distributions for the chalcogen configuration in the 4*c* position (second coordination sphere of phosphorus); open bars show the expected intensity distribution based on a statistical scenario.

however, the signals arising from the P-bonded selenium species appear significantly broadened, making their observation and quantification impossible. For this reason, Figure 11 focuses on the spectral region, in which the ^{77}Se

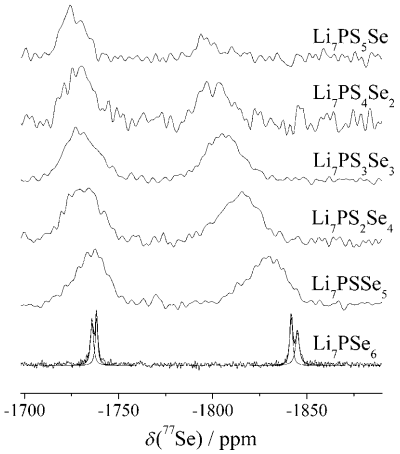

Figure 11. ^{77}Se MAS-NMR spectra of $Li_7PS_{6-x}Se_x$ solid solutions. The resonances due to the P bonded Se atoms are outside the spectral window chosen. For Li_7PSe_6, the simulated and measured curves coincide nearly perfectly.

NMR signals attributable to the 4*a* and the 4*c* sites appear. For Li_7PSe_6, a small splitting of each of these resonances is observed, indicating the presence of slightly non-equivalent selenium environments. This result is consistent with the observed splitting of the ^{31}P NMR signal, suggesting the presence of a slight structural distortion not detectable by XRD. Compared to the very sharp signals in Li_7PSe_6, the mixed chalcogenides show broadened signals owing to the additional substitutional disorder present in these phases. Although the chemical shift of the higher-frequency signal is essentially independent on composition, the lower frequency resonance shifts to higher ppm values with increasing sulfur content (see Table 6). Therefore, we attribute the latter signal to selenium species in the 4*c* positions, as the ^{77}Se chemical shift is expected to be influenced by the proximity (and thence the composition) of the nearby $(PCh_4)^{3-}$ tetrahedra. For most of the solid solutions investigated, the ratio of these two signals is found to be very close (within experimental error) to 1:1, hence confirming that the chalcogen distribution over the 4*a* and 4*c* sites is essentially statistical. Only in Li_7PS_5Se and $Li_7PS_4Se_2$ does the area ratio differ significantly from unity. Thus, there is a subtle but perceptible preference of selenium to occupy the 4*a* positions in these samples. For $Li_7PS_4Se_2$, this result is in excellent agree-

Table 6. ^{77}Se chemical shifts and fractional areas of the 4*a* and 4*c* resonances of $Li_7PS_{6-x}Se_x$ samples.

	4*a*		4*c*	
	δ [ppm]	fractional area [%]	δ [ppm]	fractional area [%]
Li_7PS_5Se	−1725	70	−1796	30
$Li_7PS_4Se_2$	−1729	57	−1801	43
$Li_7PS_3Se_3$	−1730	48	−1806	52
$Li_7PS_2Se_4$	−1731	51	−1815	49
Li_7PSSe_5	−1736	48	−1829	52
Li_7PSe_6	−1736	25	−1842	27
	−1738	(23)	−1845	(25)

ment with the ^{31}P NMR peak analysis (Figure 10). In contrast, the site preference detected for Li_7PS_5Se is much more apparent in the ^{77}Se NMR spectrum than in the ^{31}P signal intensity distribution in Figure 9. We consider the ^{77}Se NMR result, which is more direct, to be more accurate in this case.

^{6}Li solid-state NMR spectroscopy: Figures 12 and 13 and Table 7 summarise the results from ^{6}Li NMR experiments at 160 K and 150 K, the lowest achievable temperature with the equipment used, on LT-Li_7PS_6 and LT-Li_7PSe_6. The less abundant ^{6}Li isotope was chosen because the resolution in ^{6}Li MAS-NMR is significantly improved compared to that with ^{7}Li NMR, due to the weaker homonuclear dipolar interactions and second-order quadrupolar broadening effects.[10] Multiple resonances are observed in these spectra signifying the presence of distinct lithium sites with slow intersite exchanges in this range. From the assumed structure model for LT-Li_7PS_6 and Li_7PSe_6 one basically expects seven crystallographically independent Li positions with similar multiplicity (Wyckoff position 4*a* of space group $Pna2_1$). Five of them are tetrahedrally coordinated (Li2, Li3, Li4, Li5, Li7, CN = 4), one trigonal planar (Li1, CN = 3) and one nearly linear (Li6, CN = 2), see Figure 14. The tetrahedrally coordinated Li atoms form three groups: two groups of Li pairs (Li3/Li5, Li2/Li7, located on both sides of a pseudo-mirror plane) and a single Li (Li4) located very close to the pseudo-mirror plane (a real mirror plane in the HT modification). Li1 (CN 3) and Li6 (CN 2) form separate groups of single atoms due to their different coordination numbers.

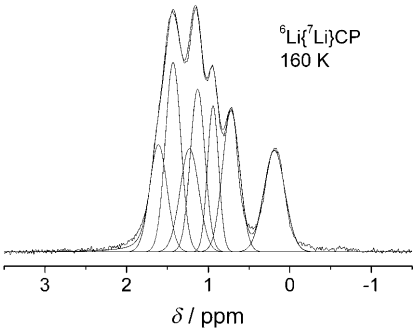

Figure 12. ^{6}Li{^{7}Li} CPMAS spectrum of LT-Li_7PS_6. The simulated and measured curves coincide nearly perfectly. The simulation is based on 7 individual components with the area ratios listed in Table 7.

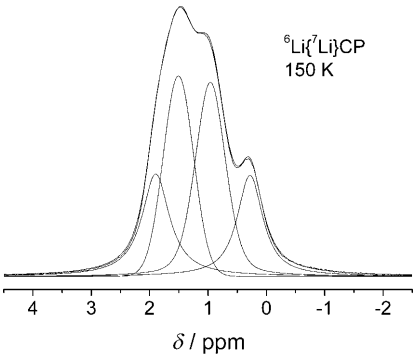

Figure 13. ^{6}Li{^{7}Li} CPMAS spectrum of LT-Li_7PSe_6. The simulated and measured curves coincide nearly perfectly. The simulation is based on 4 individual components with the area ratios listed in Table 7.

Table 7. ^{6}Li MAS-NMR line-shape deconvolutions for LT-Li_7PS_6 and LT-Li_7PSe_6.

LT-Li_7PS_6	%	LT-Li_7PSe_6	%
1.61	12.2	1.90	20
1.43	19.0	1.51	29
1.23	12.7	0.96	32
1.13	15.6	0.28	18
0.94	10.7		
0.72	15.8		
0.19	14.0		

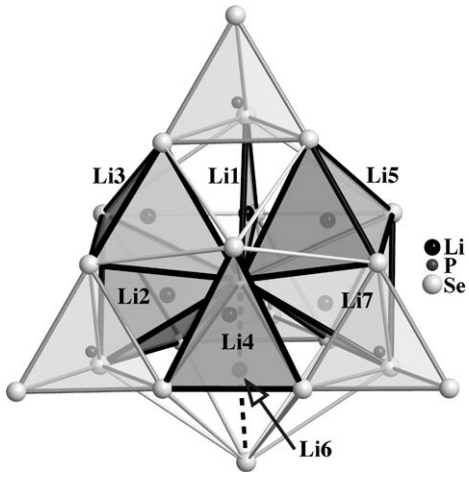

Figure 14. Crystallographically independent Li positions of LT-Li_7PSe_6 inside a ($SeSe_{16}$) Friauf-polyhedron with attached PSe_4 tetrahedra. Coordination of Li: trigonal (Li1), tetrahedral (Li2, Li3, Li4 Li5, Li7) and linear (Li6).

In both of the samples, the signal-to-noise ratio could be considerably enhanced by cross-polarising the ^{6}Li spins from the abundant ^{7}Li spin reservoir. The spectrum of LT-Li_7PS_6 reveals a number of well-resolved resonances, indicating that the exchange between the different lithium positions is slow on the NMR timescale (0.01 s). In the case of LT-Li_7PSe_6, four resonance lines can be differentiated at 150 K; however, the lower resolution suggests that the rigid lattice limit has not quite been reached at this temperature. Included in the figures are tentative peak deconvolutions. In the case of LT-Li_7PS_6, the ^{6}Li NMR spectrum can be deconvoluted into seven contributions having the area ratios listed. The higher intensity of the 1.43 ppm peak in relation to the other signals can be accounted for by a small contamination with lithium sulfide, which is evident in the XRD data. This Li_2S impurity contributes additional intensity to this spectral component, whereas all the other components appear with comparable intensities. Although the spectral deconvolution shown here is consistent with the structural model from the

X-ray data, we must note that satisfactory fits can be obtained in various other ways, as only six spectral components are resolvable without doubt. At higher temperatures, these resonances coalesce because of exchange averaging processes on the 0.01 to 0.1 s timescale, resulting in loss of resolution and the observation of single symmetric resonances at room temperature.

Experimental Section

Synthesis of Li_7PCh_6 (Ch=S, Se) and solid solutions $Li_7PS_{6-x}Se_x$: The ternary compounds Li_7PCh_6 were synthesised from stoichiometric amounts of Li_2S (prepared from LiOH and H_2S according to reference [18]) and P_2S_5 (Acros, 98%) or Li_2Se (CERAC, 99.5%) and P_2Se_5 (pre-reacted stoichiometric mixture of Se and red P) for Ch=S, Se, respectively. For solid solutions $Li_7PS_{6-x}Se_x$, P (Acros, 9.999%), S (Chempur, 99.999%) and Se (Chempur, 99.999%) were additionally used to reach the required composition. The reaction mixtures were homogenised, pressed to pellets and transferred into carbon-coated quartz glass ampoules. The carbon coating was carried out by repeated pyrolysis of acetone vapour. All experiments were carried out in an argon-filled glove box ($O_2<1$ ppm, $H_2O<1$ ppm). The respective, evacuated quartz glass ampoules were annealed for 120 h at 923 K (Li_7PCh_6) or 823 K. After the reaction, the ampoules were slowly cooled to room temperature. Li_7PS_6 is colourless. The intensity of the orange colour of the Se containing samples increases with increasing Se content. Surprisingly, we sometimes obtained the cubic HT modification of Li_7PS_6 metastable at room temperature without being able to specify the respective conditions (see below).

Powder X-ray diffraction: The air sensitive products were prepared in a glove box. The samples were ground and loaded with grease (Lithelen) between two Mylar foils (diameter=0.1 mm). The diffraction data were collected on a Siemens D5000 diffractometer (Cu-$K_{\alpha1}$ radiation, Ge monochromator). High-temperature measurements were carried out in evacuated quartz glass capillaries (diameter=0.2 mm) on a STOE Stadip diffractometer. The data analyses were performed using STOE Software package WINXPOW.[19]

Single-crystal investigations: Crystals of Li_7PCh_6 with an appropriate size were selected in a glove box equipped with a microscope, transferred into capillaries, which were evacuated and sealed. The capillaries were mounted on an imaging plate diffraction system (STOE IPDS I) and measured using graphite monochromatised $Mo_{K\alpha}$ radiation ($\lambda=$ 0.71973 Å). The X-ray single crystal structure determinations of HT-Li_7PCh_6 crystals are based on measurements at 503 K (Ch=S) and 453 K (Ch=Se). This was achieved by slow heating (10 $K min^{-1}$) of twinned LT crystals directly on the diffractometer starting from ambient temperature above the phase transition. The STOE IPDS program package[20] was used for the data evaluation. For the structure solution and refinement, the programs SHELXS-97[21] and SHELXL-97[21] were used. In rare cases, we obtained Li_7PS_6 in the cubic HT form metastable at ambient temperature far below the phase transition. These products always contained significant amounts of unreacted Li_2S and show, in contrast to "normal" reaction products, only very small crystals of the argyrodite. One of these crystals was measured at 273 K. The result of the structure refinement does not show any anomalies compared to the measurement at 503 K. The X-ray powder pattern of such samples agrees with the calculated ones. The volume (976.93(8) $Å^3$) is significantly higher compared to the volume of the assumed orthorhombic LT modification (969.26(4) $Å^3$). This suggests a higher stability of the latter.

Further details of the crystal structure investigations can be obtained from the Fachinformationszentrum Karlsruhe, 76344 Eggenstein-Leopoldshafen, Germany (fax: (+49)7247-808-666; e-mail: crysdata@fiz-karlsruhe.de) on quoting the depository number CSD-421130 (Li_7PS_6) and CSD-421131 (Li_7PSe_6).

Thermal analyses: Thermal analyses were conducted in pressure resistant stainless steel crucibles on a SETARAM DSC 131 (heating and cooling rates: 7 $K min^{-1}$).

X-ray analysis: EDX (energy dispersive X-ray) analysis was used to semi-quantitatively (Li disregarded) check the ratio of phosphorus/sulfur/selenium and to prove the absence of silicon (quartz glass ampoule), which is important due to the existence of silicon-containing argyrodites.

Solid-state NMR spectroscopy: The ^{31}P NMR experiments were conducted on a Bruker DSX 400 spectrometer working at a Larmor frequency of 161.92 MHz. A Bruker MAS WVT probe (4 mm stator) was used and the duration of the 90° pulses was 2.8 μs. Data were measured using single-pulse acquisitions at a spinning speed between 11 and 15 kHz. The relaxation delay was between 60 s and 120 s. Since the samples are highly moisture sensitive, the rotors were packed in a glove box and spun with nitrogen. The relative peak areas were quantified by signal integration, taking spinning sidebands into account. In certain cases, a more detailed peak deconvolution was done using the DMFIT programme. All chemical shifts are reported relative to 85% H_3PO_4. ^{77}Se NMR spectra were obtained at 76.3 MHz, with 90° pulses of 3 μs in length and relaxation delays of 40 s using a rotor-synchronised Hahn spin echo sequence at a spinning frequency of 12 kHz. Spectra are referenced to 96% selenic acid solution. $^6Li\{^7Li\}$ cross polarisation magic angle spinning (CPMAS) experiments were performed by using a 4 mm Bruker double resonance probe at a Larmor frequency of 54.2 MHz and 155.5 MHz for ^6Li and ^7Li, respectively. The methodology was first described in ref. [22]. The MAS frequency was set to 5 kHz and the 90° pulse length for both nuclei was 7.6 μs. The contact time was 9 ms for Li_7PS_6 and 10 ms for Li_7PSe_6. For both samples, a relaxation delay of 10 s was used.

Acknowledgements

Funding by the Deutsche Forschungsgemeinschaft under programme SFB 458 "Ionic motion in disordered materials" and the project "Li-Argyrodite" DE 365/12—1 is most gratefully acknowledged.

[1] W. F. Kuhs, R. Nitsche, K. Scheunemann, *Acta Crystallogr. Sect. B* **1978**, *34* 64–70.
[2] E. E. Hellstrom, R. A. Huggins, *J. Solid State Chem.* **1980**, *35*, 207–214.
[3] H.-J. Deiseroth, S.-T. Kong, H. Eckert, J. Vannahme, C. Reiner, T. Zaiß, M. Schlosser, *Angew. Chem.* **2008**, *120*, 767–770; *Angew. Chem. Int. Ed.* **2008**, *47*, 755–758.
[4] H.-J. Deiseroth, S. T. Kong, M. Schlosser, C. Reiner (University of Siegen), DE-102007048289 A1, **2007**.
[5] M. Tatsumisago, S. Hama, A. Hayashi, H. Morimoto, T. Minami, *Solid State Ionics* **2002**, *154–155*, 635–640.
[6] E. Gaudin, H. J. Deiseroth, T. Zaiß, *Z. Kristallogr.* **2001**, *216*, 39–44.
[7] J. v. Unterrichter, K.-J. Range, *Z. Naturforsch. B* **1978**, *33*, 866–872.
[8] E. Gaudin, F. Boucher, V. Petricek, F. Taulelle, M. Evain, *Acta Crystallogr. Sect. B* **2000**, *56*, 402–408.
[9] E. Gaudin, V. Petricek, F. Boucher, F. Taulelle, M. Evain, *Acta Crystallogr. Sect B* **2000**, *56*, 972–979.
[10] H. Eckert, Z. Zhang, J. H. Kennedy, *Chem. Mater.* **1990**, *2*, 273–279.
[11] R. H. P. Francisco, T. Tepe, H. Eckert, *J. Solid State Chem.* **1993**, *107*, 452–459.
[12] J. F. Brice, *C. R. Seances Acad. Sci. Ser. C* **1976**, *283*, 581–584.
[13] M. Evain, E. Gaudin, F. Boucher, V. Petricek, F. Taulelle, *Acta Crystallogr.Sect. B* **1998**, *54*, 376–383.
[14] R. Mercier, J. P. Malugani, B. Fahys, G. Robert, J. Douglade, *Acta Crystallogr. Sect. B* **1982**, *38*, 1887–1890.
[15] B. C. Chan, P. L. Feng, Z. Hulvey, P. K. Dorhout, *Z. Kristallogr. New Cryst. Struct.* **2005**, *220*, 11–11.
[16] P. T. Cunningham, S. A. Johnson, E. J. Cairns, *J. Electrochem. Soc.* **1971**, *118*, 1941–1944.

[17] R. Maxwell, D. Lathrop, D. Franke, H. Eckert, *Angew. Chem.* **1990**, *102*, 950–951; *Angew. Chem. Int. Ed. Engl.* **1990**, *29*, 882–884.
[18] K. Yamamoto, N. Ikeda (Furukawa CO LTD), EP0802159, **1997**.
[19] WINXPOW, Version 1.08. STOE & Cie GmbH Darmstadt, **2000**.
[20] STOE&CIE, IPDS Software, Version 2.93, Darmstadt.
[21] G. M. Sheldrick, *Acta Crystallogr. Sect. A* **2008**, *64*, 112–122.
[22] L. van Wüllen, T. Echelmeyer, H.-W. Meyer, D. Wilmer, *Phys. Chem. Chem. Phys.* **2007**, *9*, 3298–3303.

Received: November 2, 2009
Published online: March 26, 2010

